Pulsed thermography digital motion stabilization for the Unmanned Vehicle inspection of solar farms and GFRP wind blades through UAVs and UGVs

Beñat Urtasun*[a], Pablo López de Uralde[a], Karlos Velar[a], Eider Gorostegui-Colinas[a]
Joonal Neelov[b], Steve Wright[b], Matthew Studley[b]
Pedro Lima[c], Alberto Vale[c], Meysam Basiri[c]

[a] LORTEK Technological Centre, Basque Research and Technology Alliance (BRTA),
Arranomendia Kalea, 4A, Ordizia, 20240, Spain

[b]University of West England, Frenchay Campus, Coldharbour Lane, Bristol, BS16 1QY, United Kingdom

[c]Instituto Superior Técnico Lisboa, Av. Rovisco Pais, 1-1049-001 Lisboa

ABSTRACT

The quality control of structures and fuselages in both the wind-turbine and solar sectors is a fundamental part that allows a lifetime assessment of their elements, from its initial assembly to the recurring inspection cycles. Automating the active thermography on this scale, cannot be achieved with conventional industrial robots. Unmanned vehicles, such UAVs and UGVs, present distinctive advantages that should certainly be exploited, but, its inherent static motion is one of the main stumbling blocks towards its use in an active thermography inspection. In this paper, a two-step digital stabilization scheme has demonstrated its efficacy in real defects located in both a wind blade and solar panel. The combination of a feature-based registration algorithm and a dense parametric optical flow direct alignment has enabled the pseudo-static reconstruction of the thermograms. The adopted experimental methodology, employing a robot with both halogens and IR camera, subjected to random motions with varying speed and amplitudes, has allowed a direct repeatable comparison of static and stabilized phase images. The phase image contrast comparison of both static and dynamic tests, have been carried out on a flat bottom hole (FBH) wind blade GFRP sample, showing nearly identical phase contrast with marginal differences. Likewise, a real GFRP wind-blade impact delamination defect has also reached a close phase contrast regarding its counterpart, albeit with a decreased contrast. Additionally, the registration algorithm has been used to stitch the individual frames, derived from a dynamic recording of an electroluminescent solar panel, to allow for a unified detection and mapping of defects.

Keywords: Thermography, Electroluminescence, UAV, UGV, Inspection, Digital Stabilization, optical flow, pseudo-static reconstruction, stitching, GFRP, fuselage, solar panel, wind blades, wind turbines, polycrystalline.

1. INTRODUCTION

Nowadays, with the competition that exists and the quality that is required in all the products that companies develop and need to maintain after, it´s becoming more and more necessary to have robust quality controls in their equipment and launch them as fast as possible in order to reduce cycle times.

If we focus on the need for inspection, more and more sectors are tending to change traditional destructive inspection methods for Non-Destructive Testing (NDT) techniques. Since on many occasions, the object to be inspected is in good conditions and only preventive maintenance is required.

Focusing on the object of this paper, in wind blades, for example, which are elements that are located in the windmills at great heights, also the application of traditional NDT implies a complexity that must be solved. Different types of wind turbine blade defects have been reviewed in the past [1]. Some defects, such as the leading edge erosion can reduce the efficiency of up to a 10% [2], mainly caused by the liquid drop-let impingement of the blade tip which reduces the aerodynamic performance by creating drag. Some other defects, like internal delamination, originated from a factory defect or external impact, might even increase the risk of collapse, [3].

Photovoltaic (PV) defects, are also well studied, [4]. Most PV defects, can be categorized whether as intrinsic or extrinsic ones. The former can be associated to the underlying material that might cause a decreased recombination efficiency related to grain-boundary dislocations. This inhomogeneity in turn, produces a high recombination rate mainly due to a higher local dopant density usually associated to defects produced at the foundry itself. Other kinds of PV intrinsic defects, can be associated to metal contaminations or avalanche-breakdowns caused by anomalies during the etching process, among others. Extrinsic PV defects are commonly associated to external impacts, some have been named as "broken fingers" [5], which are typically associated to contact grid problems, mainly caused by external impact or deficient electrical contact between cells. Additionally, it is also worth noting that the detectability of the semiconductor intrinsic defects are more sensible to the subjected temperature [4]. Taking into account the array of PV defects surfacing in the solar fields, it is necessary to find fast and efficient ways to perform the panel inspections. On the one hand, active thermography based on halogen lamps has been studied with very modest results, caused by the external clear protection glass present on the final PV units, partially altering heat diffusion. These particular tests have not been included in this paper. On the other hand, electroluminescent (EL) excitation has shown very good results in the detection of both type of defects, with prompt infrared radiation, allowing for still images defect detection.

Particularizing the inspection of any Unmanned Vehicle while fusing different sensors has progressively stepped towards a full unassisted automated inspection, such as the one shown in [6]. Some state of the art reflection terahertz wave inspection systems are showing promising results on the inspection of surfaces, providing high-speed volume inspections. There are certainly very promising use cases, but one of its main drawbacks it's an extreme sensitivity of the physical distance of the device, relative to the surface [7]. On the contrary, even the limited depth of field of IR cameras is several orders of magnitude above it. The mapping of the thermal evolution into each framed physical point of the inspected surface is most definitely a prerequisite in most active thermographies techniques. On the other hand, passive thermography inspection wind turbine blades in drones can be used in the right conditions, where a natural diffusion is produced by the sun over periods surpassing the 30 minutes mark [8]. The still images are then manually analyzed by experienced operators, that are trained to discern certain features in the ever varying thermal conditions associated to weather, ambient temperature, surface humidity and lighting conditions, among many other factors. Active thermography allows for a controlled thermal diffusion, enabling the creation of predictable patterns to be easily analyzed on an automatic fashion. The natural oscillations of any UAV, can certainly be compensated with the drone control itself, as well as gimbals sustaining the cameras, all referenced by a local or global positioning systems, subjected to their own variances. Nonetheless, some systems have reported a 1 cm accuracy [9]. Typical spatial resolution of 500μm/pixel is hardly ever attained by physical stabilization alone. A precise and robust digital motion stabilization is certainly required for a viable option.

Following sections are structured in the following manner:
- Technologies description: presents a short summary of the thermographic technologies used
- Experimental: test methods are exposed
- Stabilization algorithms: details the core technique and the scheme developed.
- Results: analyze and compare ideal static measurements, in respect of dynamic thermographies
- Conclusions and future work

2. TECHNOLOGIES DESCRIPTION

In the following section a short summary of the technologies used is presented. Note that the specific digital stabilization related work is depicted in 4.1.

2.1 Active thermography

Several excitation techniques are employed in active thermography for NDT defect detection. Those excitations can be optical (laser or lamp based), ultrasonic waves or electric current. The basics for all of them are similar: the sample to be inspected is subjected to an external excitation and a thermal camera captures the heat propagation along the sample. This propagation depends on the thermal properties of the material, and the existence of anomalies lead to differences in this distribution that derive in temperature differences in the surface.

Within optical excitations, we can distinguish two ways, one based on laser, and the other one on lamps. The object of study of this article is in the lamps, specifically in halogen lamps.

When using halogen lamps, two main employed techniques are: Lock-in, which generates a cycle of a predetermined number of periodical heat waves (sinusoidal, rectangular, triangular…) and pulse heating, which employs only one pulse (usually square shaped). This second technique has been chosen for this work.

When the pulse heat flux is applied to the sample surface, lateral and internal heat flow is generated into the sample. In sound zones, the heat distribution is not affected and is maintained uniform. If the sample has defects, superficial or internal, a localized high temperature region appears on the sample surface just above the defect due to the insulation effect [10]. These differences on heat distribution and propagation can be observed when applying Fast Fourier Transform, manifesting its effect, mainly on the phase image.

2.2 Electroluminescence EL

The other technique used in this paper, is the electroluminescence (EL), which is a powerful tool to characterize the local and overall electrical and electronic properties of photovoltaic (PV) modules. EL produces a prompt infrared radiation allowing for the still IR images processing, without even recording its associated thermal diffusion. Limited by both the spatial resolution of the camera, and diffusion length of carriers conforming the cell itself, this is a very scalable technique. For this reason, EL is also usually used to characterize not only single solar cells, but also entire modules and even large PV arrays. Most commonly, EL images provide qualitative information about the pure existence of defective parts of cells or modules in a photovoltaic system. Sometimes, from the shape of luminescence patterns it is also possible to deduce the type of defects. Moreover, if EL measurements are combined with other characterization techniques, it is sometimes also possible to quantitatively predict the electrical performance of the cell, module, or module string [11, 12].

The EL effect itself is associated to local voltage, which causes an increase of the radiation next to the current injection point. It is true that the voltage drops proportionally to the distance regarding current injection point, but in most PV modules the connection layout allows for an homogeneous current injection. As a result, any localized radiation anomaly is usually a reliable indicator of a certain type of defect. Some other aspects can alter the junction current, such as:
- The ideality factor and saturation current density of the diode
- The shunt currents that circumvent the diode.

2.3 Fast Fourier Transform (FFT)

The thermal image sequences processing technique based on FFT enables to change from time domain to frequency domain, analyzing the time evolution of the image sequence captured by pulsed infrared thermography applying the discrete one-dimensional Fourier transform pixel-by-pixel. The FFT is a collection of algorithms for fast computation of the Discrete Fourier Transform (DFT) and is based on factorizations to reduce the transforms complexity. The one-dimensional function decomposes the surface thermal signal evolution in two components: amplitude (modulus) and phase (phase delay), both symmetrical about the frequency f = 0 Hz (n=N/2). The discrete FT (DFT) can be written as:

$$F_n = \Delta t \sum_{k=0}^{N-1} T(k\Delta T) exp^{(-j2\pi nk/N)} = Re_n + Im_n \qquad (1) \qquad A_n = \sqrt{Re_n^2 + Im_n^2} \qquad \emptyset_n = t \qquad (2)$$

where n designates the frequency increment, Δt is the sampling interval; and Re and Im are the real and the imaginary parts of the transform, respectively. The frequency components can be derived from the time spectral as $f_n = n/(N \cdot \Delta t)$, where N is the total number of frames in the thermal sequence.

3. EXPERIMENTAL

3.1 Samples employed: Description and defectology

Two types of samples have been inspected, first, a GFRP wind turbine blade and second a polycrystalline solar panel. Wind turbine fragment corresponds to a 1.5x1m section from the tip area. The inspected portion has a 5mm thickness, as shown in Figure 1. It presents multiple real defects, such as a leading edge erosion as well as an internal delamination, caused by a real impact. The latter defect is the one that has been chosen to be subjected to the tests. Additionally, a fragment has been extracted to Flat Bottom Hole (FBH) its back. Compounding the holes drilled parallel with the surface curvature has resulted in small deviation of the actual depths reflected in Figure 2.

a)   b)

Figure 1. Eolic blade employed for the inspection. a) cross-section, b) highlighted delamination defect

	C1	C2	C3	C4	
R1	2.2	2.2	1.8	1.7	
R2	2.4	2.5	2.5	2.5	DEPTH
R3	2.4	2.5	2.5	2.5	
R4	4.6	5	5.4	6.1	
	2.5	1.5	1	0.5	Ø

a)   b)   c)
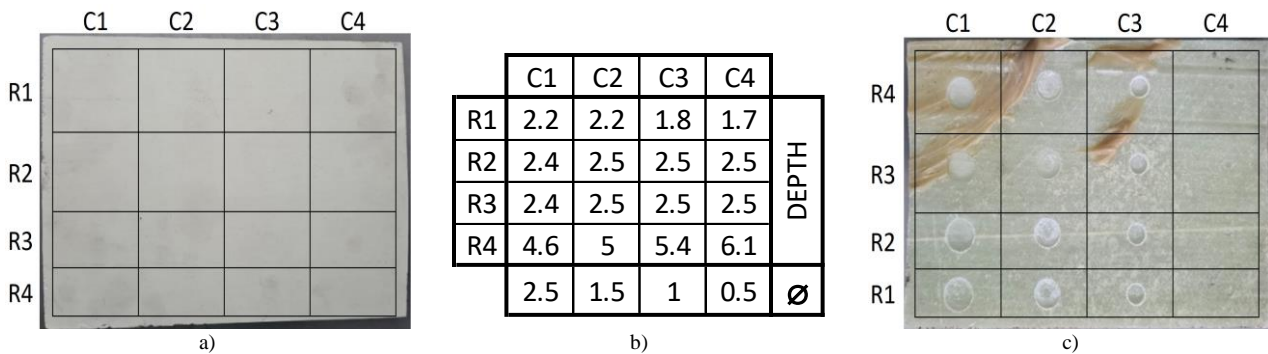
Figure 2. Flat bottom holes (FBH) on wind blade. a) external face, b) holes depth and diameters, c) internal face

The solar panel employed has the following characteristics:

Type: polycrystalline	Maximum power: 360W	Isc: 9,7A
Vmp: 39,2V	Imp: 9.18A	Voc: 47,9V

As previously mentioned, the external clear glass layer present in the final PV units, certainly limits the effectivity of alternative techniques that won't be shown in this paper. The defects present in the tested panel originate from the solar power plant itself, mainly derived from physical impacts. Cracked cells underperform and in some cases during normal operation, they can produce hot spots that progressively affect the panel.

3.2 Equipment

For the inspection of the wind blade, active thermography with halogen lamps as external excitation has been used, as a non-destructive testing technique. As can be seen in Figure 3, the setup consisted of two-2000W halogen lamps (adjustable power) mounted on a 6-axis Kuka KR30-HA, together with a FLIRx6540sc refrigerated camera. The relative position between the camera and the lamps is fixed, so they move together. This configuration is designed to replicate a future system mounted on a drone, in order to simulate real conditions for the tests.
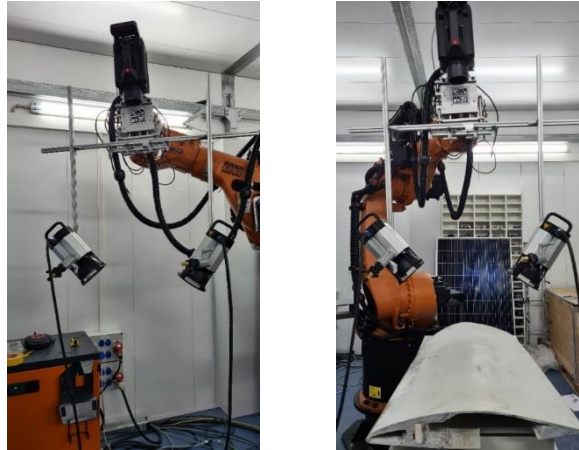
Figure 3. Set up for active thermography tests

In the case of the solar panel, the technique employed has been electroluminescence. The panel has been connected to a power supply that provides the necessary voltage to excite it. In order to keep it fixed, it has been mounted on a rotary table coordinated with the robot, while using a Basler acA640-120gm camera, as shown in Figure 4. Even if the camera is not the optimal for the acquisition of the aforementioned $0.8-2.5\mu m$ wavelength radiation, caused by its declined quantum-efficiency in the NIR, it has offered good results used in the dark. While the usage of a low-pass filter has not been evaluated, it could easily amend this situation. The camera has been mounted on the robot in a similar fashion as the thermal one.

Since the detection of defects on the electroluminescent panel does not require the measurement of its thermal diffusion, ideally a single still image for each area, would be sufficient. Both static tests and dynamic ones have swept the panel following a raster path, easily replicated by most UGVs. Static test has stopped at each individual cell, while the dynamic has followed through with a continuous 10Hz recording.
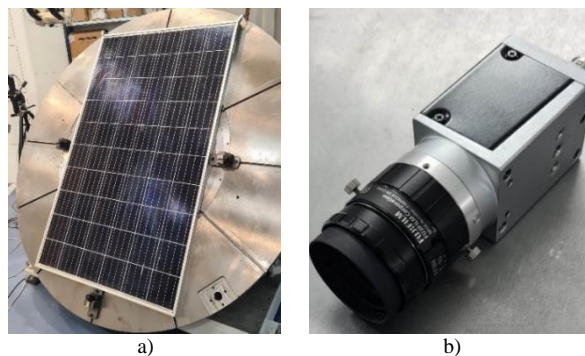

a)   b)

Figure 4. a) solar panel positioning on rotatory table, b) visible and NIR Basler camera

3.3 Description of tests

As previously mentioned, the main focus of the tests resides in the validation and comparison of motion stabilized thermographies regarding its static counterparts. One of the most common ways to reduce the dimensionality of the recording sequence, is based on the detection of defects highlighted by the phase image derived from the pixel-wise time

series FFT. A simple metric to evaluate the defect signal is the phase contrast, or $\Delta Phase$, of the defective area regarding the neighboring sound one. Aiming for the direct comparison, a set of tests has been defined with identical excitation and capture parametrization while, at the same time, recurring to different motions of varying velocities and amplitudes.

Down below, are presented the different aspects of the experiments.

3.4 Excitation and acquisition parameters

Both the FBH and impact delamination of the wind blade have been subjected to the pulsed thermography, with the recording synchronized for different heating periods, acquiring both the heating and cooling.

As a general criterion, it has been established that the recorded cooling corresponds to a 75% of the total recording time, as shown in Figure 5. This extended capture allows for the phase evaluation at different cooling periods, pondering its diminishing contribution to the phase contrast.

Lamps have been capped at 75% power of its maximum power to avoid the saturation of the thermal sensor throughout the whole set of heating periods. The frame rate has been set at 12Hz, integration time at a constant $100\mu s$. Note that all the excitation and capture parameters have remained the same for both the static and dynamic tests.
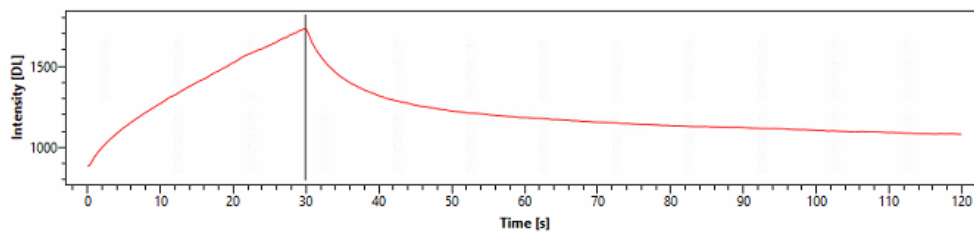

Figure 5. Temporal evolution of the intensity values during a measurement

Third set of tests involves the detection of solar panel defects by electroluminescence. A standard 72-cell polycrystalline PV module, subdivided in three sections connected in parallel, has enabled the continuous supply of 19V for each section. This direct voltage produces 9A of current, or 171W of consumption.

During all tests, both static and dynamic values have remained fixed. The camera's frame rate, in dynamic tests, has been fixed at 10fps. Due to the limited NIR sensitivity, an extended 500ms exposure is required.

3.5 Dynamic motions

On real inspections using both UAVs and UGVs, develop static measurements is a big challenge. Both systems are affected by meteorological conditions (such as wind for the UAVs), ground instabilities or even mechanical vibrations of the system. Many publicly available drone telemetry data set, such as [13, 14], compiles the telemetry of numerous sensors, some simulated, other based on real measurements, but they mainly designed for the training of models for the autonomous navigation or Simultaneous Localization and Mapping problems (SLAM). Only navigation trajectories are included in the aforementioned datasets- This deficiency has motivated the emulation of the motions of varying amplitude and velocities in an industrial robot, to factor its viability in different scenarios.
Simulated trajectories have been executed on a 6-axis industrial robot. Two different approaches types of motions have been considered, as shown in Figure 6:
- Circular motion with an overlapped noise as shown of a 45mm radius
- Random distribution of points on a 2d bounded box of 45mm

Note that the movement of the robot has been constrained to the horizontal plane with the camera facing downwards, and an additional oscillating vertical rotation has been added. Varying velocities, first by changing the spacing of the discretized points of the trajectory coupled with the use of point to point motions, ensures varying physical camera velocities. On top of that, in the subsequent digital stabilization process, the skipping of frames has served to emulate abrupt accelerations. The skipping of frames at a varying rate has not been contemplated, as the irregular temporal resolution would certainly

distort the actual phase image derived from it. Certainly, an intermediate post-processed image-space interpolation could be applied countering this eventual situation.
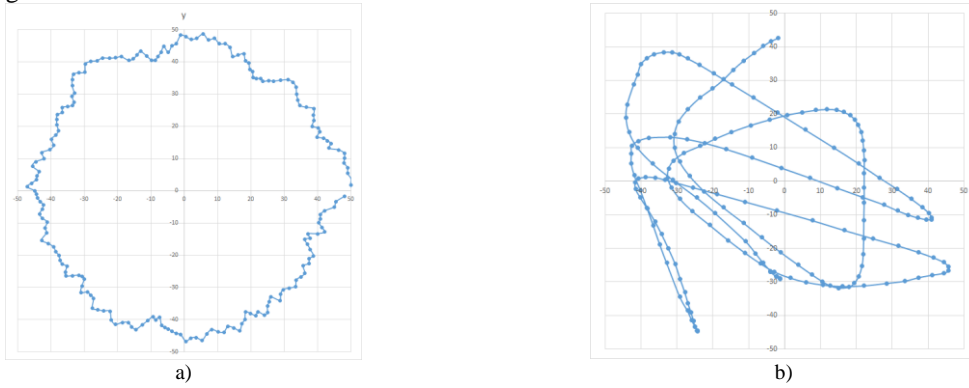

Figure 6. horizontal plane trajectories to simulate drone movement in mm. a) circular with added noise. b) random trajectory

Contrary to the pulsed thermography, the EL carried out in the solar panel does not require fixed static recording. The motion has consisted in a raster trajectory along the solar panel with an overlapped sinusoidal noise of 45mm.

4. STABILIZATION ALGORITHMS

4.1 Related work

In this paper, a robust digital stabilization system has been developed, specifically geared towards the reconstruction of a pseudo-static thermography. Ideally, each pixel of the reconstructed thermogram must map the same physical point during the whole pulse and subsequent cooling phase. Depending on the type and magnitude of the misalignment, its effects could range from a simple added noise, to a complete misrepresentation of the underlying thermogram.

Many devices are commonly used to solve or minimize this particular problem in many optical drone inspections. Most common systems recur to multiple axis gimbals, sustaining the camera itself, such as the one shown in [15]. Other systems have used an accelerometer to digitally stabilize the image by estimating its relative movement based on an extrinsic camera calibration regarding the sensor [16]. These methods are able to stabilize the image, mitigating the problem, but hardly ever reaching a pixel-wise alignment. To achieve a robust registration, it is necessary to employ a digital stabilization technique.

Contrary to other forms of dynamic line scan thermographies [17], in this scenario the motion of the camera relative to the inspected object is unknown, and cannot be subjected to a linear interpolated shift of the motion. Aggravated by the limitations of currently available uncooled IR cameras, requiring high aperture ratios, the resulting depth of fields is constricted [18], requiring an stable positioning. This limitation allows the assumption of a constant scale of the object during the whole recording. Digital image stabilization for UAV has been employed in many situations before for visual inspection, with different sets of requirements. The main problem in this particular scenario relies in the image registration between adjacent frames, most notably subjected to different varying intensity derived from the halogens and reflections caused by the environment. Image registration techniques are divided in two groups, one based in key points and feature matching, inherently sparse, used in a vast array of applications, and the other based on direct dense matching. Most common key point feature matching algorithms [19, 20, 21] are particularly efficient and able to register large perspective deviations, but given its sparse nature they lack the accuracy of the latter.

Some dense matching techniques relies on the fact that the 2D Fourier transform of a shifted signal have similar magnitude, but a linear variation of the phase. This enables a whole image registration based on the phase correlation, as shown in [22]. Alternatively, the most extended dense registration, relies in the optical flow, first exposed by Lucas-Kanade [23]. The optical flow equation, for 1D signals, would assume: $I_0(x) = I_1(x + \Delta x)$ allowing the derivation of the optical flow equation as shown in (3) and (4).

$$I'_1(x) \approx \frac{I_1(x + \Delta x) - I_1(x)}{\Delta x} \quad (3)$$

$$E_{LK_{1d}} = \sum_i \left(I'_1(x)\Delta x - \left(I_0(x) - I_1(x) \right) \right)^2 \quad (4)$$

Generalizing for 2 dimensions.

$$E_{LK_{2d}} = \sum_i \left(\left(\frac{\partial I_1(x)}{\partial x}, \frac{\partial I_1(x)}{\partial y} \right) \cdot \Delta x - (I_0(x) - I_1(x)) \right)^2 = \sum_i (A \cdot \Delta x - b)^2 \quad (5) \quad \Delta x = (A^T A)^{-1} A^T \Delta x \quad (6)$$

Note that $A = \nabla I$ and $A^T A = J = H$, is the gradient and Jacobian respectively, in this particular case it coincides with the Gauss-Newton approximation of the Hessian. The LS regression shown in (6) enables an iterative gradient descent increasing its accuracy. The different variants of the optical flow minimization equation, have tried to reject outliers, diminishing its contribution in the objective function recurring to different function compositions, such as the Geman–McClure, used in [24], which in turn, enables the masking or outlier premature removal. Others have weighted the equation of higher gradient values [25]. To enable different types of motions, the optical flow generalization, described in [26], alters the Gauss-Newton Hessian approximation, $H = J^T J$, using a *correspondence or motion field*, from the Euclidean image space, x, to the parametric, p, associated to the motion model. Employing a simple Euclidean rigid transformation, with $p = (t_x, t_y, \theta)^T$, results in the following mapping (7).

$$x' = T_{euclid}(x) = \begin{pmatrix} c\theta & -s\theta & t_x \\ s\theta & c\theta & t_y \end{pmatrix} \begin{pmatrix} x \\ y \end{pmatrix} = \begin{pmatrix} x\,c\theta - y\,s\theta + t_x \\ x\,s\theta + y\,c\theta + t_y \end{pmatrix} \tag{7}$$

Taking into account the generalization described in [26], the Jacobian, J, associated to the correspondent point has the following form: $J = \nabla I_1(x) \cdot \partial x / \partial p$. Its particularization to the Euclidean model is derived as follows (8):

$$\frac{\partial x'}{\partial p} = \frac{\partial T(x)}{\partial p} = \begin{pmatrix} 1 & 0 & -xs\theta - yc\theta \\ 0 & 1 & xc\theta - y\,s\theta \end{pmatrix} \tag{8}$$

The Euclidean parametrized optical flow is shown in (9).

$$E_{LK_{2d}} = \sum_i \left(\nabla I_1(x) \cdot \frac{\partial x'}{\partial p} \Delta p - (I_0(x) - I_1(x)) \right)^2 = \sum_i (J \cdot \Delta p + e_i)^2 \tag{9}$$

Resulting in the following Hessian (10) and residual vector (11):

$$A = J^T J = \sum_i \left(\left(\frac{\partial x'}{\partial p}(x_i) \right)^T (\nabla I_1(x_i))^T (\nabla I_1(x_i)) \left(\frac{\partial x'}{\partial p}(x_i) \right) \right)^2 \quad (10) \qquad b = \sum_i -e_i \left(\frac{\partial x'}{\partial p} \right)^T (\nabla I_1)^T \quad \overset{(11}{)}$$

4.2 Stabilization Algorithm

The main goal of this algorithm is to obtain a phase image as close as possible to the static thermography. This requires a robust image stabilization, achieved by combining an initial sparse feature image registration, based on the Lucas-Kanade Sparse Optical Flow implemented with pyramids, shown in [27], and subsequently a dense optical flow based on the parametric Euclidean motion previously exposed, based on [26]. This second fine approximation, allows a very precise alignment even in images with few corners and small gradients, very common in the late cooling phase due to the associated thermal diffusion. The flow shown in Figure 7 is broken down in multiple phases. Starting with the stabilization of the adjacent frames, both contiguous frames are equalized with the same linear transformation. Second, Shi-Tomasi corner detector is applied in to the previous frame. Third, sparse optical flow matching [27] is employed, as shown Figure 8. If the number matched pairs does not attain a certain number, the previous pair-wise transformation is employed as an initial guess, alternatively the Euclidean transformation is estimated using a simple trimmed mean, that serves to warp the previous frame and masking both frames to its overlapped section. The final direct iterative dense alignment is executed, first by precomputing once the parametrized hessian matrix, previously exposed. Upfront precomputation of the Hessian, with $O(n^2)$ complexity, [26], enables an increased efficiency used to further refine the alignment accuracy with a higher number of iterations. Image difference and its associated residual vector are computed to perform LS regression of $\Delta p = (t_x, t_y, \theta)$. Updating the relative Euclidean transformation, the iterative process is stopped based on its convergence, or number of iterations. As show in Figure 9 the convergence is shown with the reduced image difference. From a) to b), the difference is 57 pixels horizontally and 177 pixels vertically. From b) to c), -1 pixel horizontally and 1 pixel vertically The entire process is repeated for the subsequent pairs of frames, creating a set of adjacent transformations. As with any gradient descent algorithm, the convergence to irrelevant local minima is possible [28], and in this particular problem the instantaneous velocity is assumed to be smooth. The classical method to alleviate this problem, [29], consist in smoothing

the resulting image-space trajectory. In this case a simple exponential rolling average, EMA, has been applied with a narrow $\beta = 0.95$. In our stabilization scheme, the final image-space trajectory, can be used for both stitching thermographies, and stabilizing the complete sequence. The complete thermogram must segment the incomplete image section, this particular requisite, is carried out by intersecting the whole warped mappings, W, associated to the sequence.
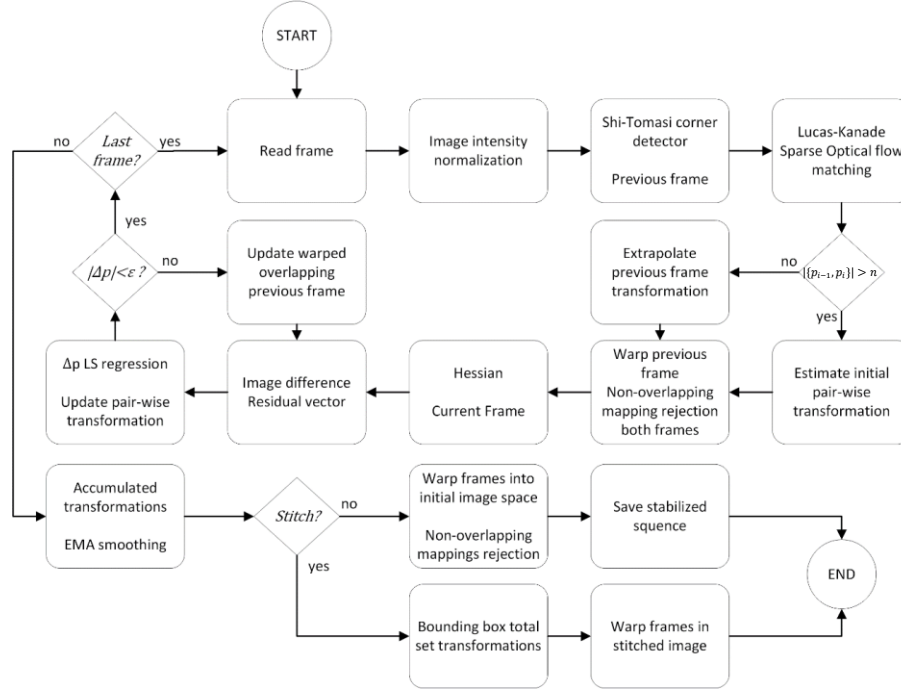

Figure 7. Motion stabilization flow chart
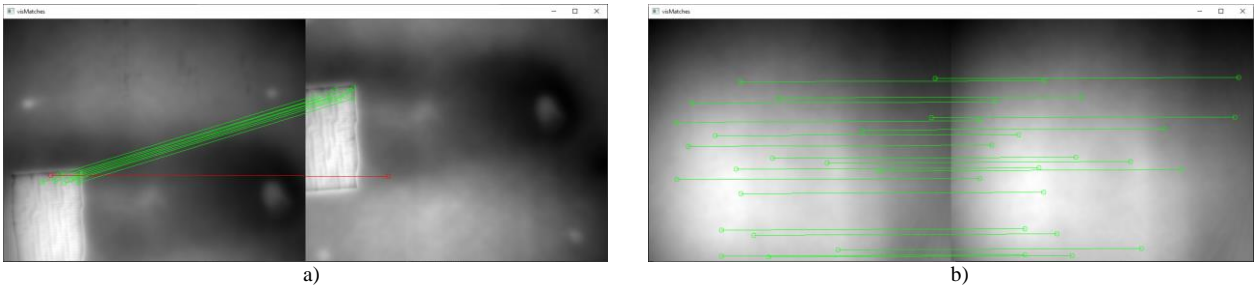
Figure 8. Example of sparse optical flow feature matching, in two different cases of the same wind turbine blade. a) Leftmost has an artificial addition with sharp gradients, allowing a robust feature extraction, notice an outlier signaled in red, b) has an unaltered homogeneous surface with a similar matching ratio, nonetheless presenting a higher variance in its relative displacement.
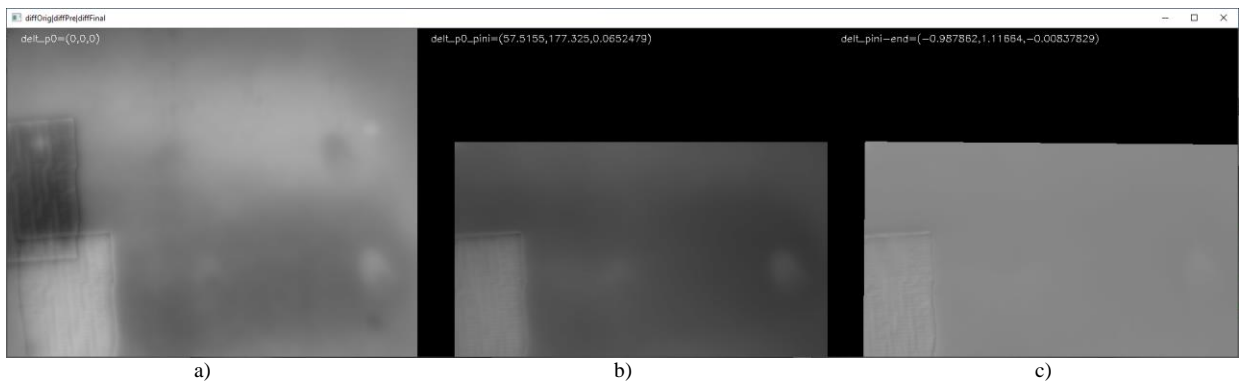

Figure 9. Image differences in distinct phases of the pair-wise registration, a) initial, b) coarse, c) final alignment.

5. RESULTS

The comparison of static and stabilized thermographies has focused in measuring the difference in the derived phase contrast of a FBH and real delamination sample.

5.1 Flat Bottomed holes on Eolic blade

Below is a summary of the measurement parameters employed.
- Resolution: 640x512
- Recording speed: 12Hz
- Pulse length: 30s
- Pulse power: 75% (2x2000W)
- Integration time $100\mu s$
- Frame interval FFT evaluation: 360-1000 (30-83.33s, cooling)

In Figure 10, vertical cuts along the first phase 0.02Hz are presented, comparing both static and random motion stabilized equivalents. A small phase contrast decrease can be observed in the random trajectory.
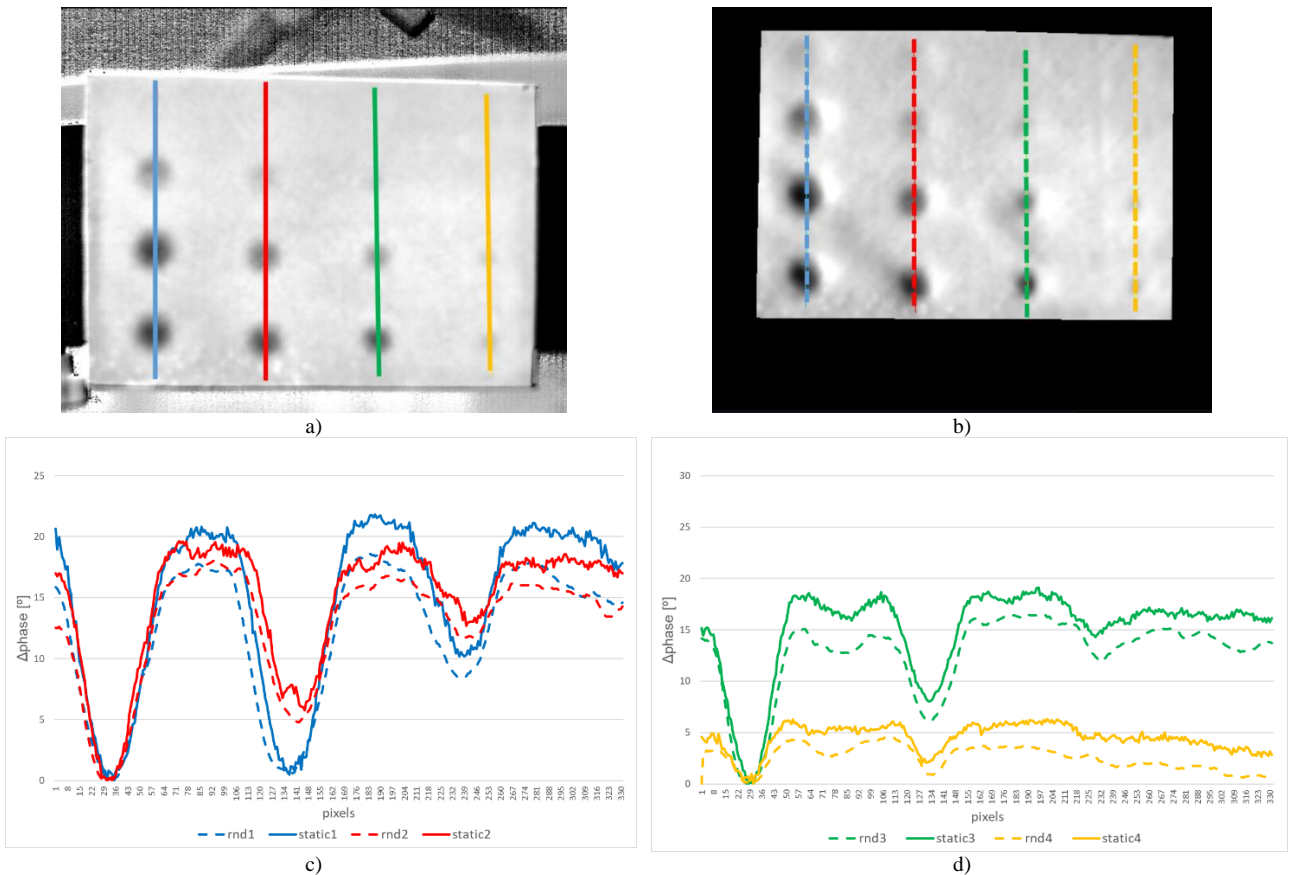

Figure 10. Flat bottom hole phase image (0,02 Hz) for static a), and random motion stabilized b) inspections. c) and d) shows corresponding phase along the colored curves.

Looking at the horizontal phase profile, shown in Figure 11 a) and c), the outer pixels adjacent to the holes have clear deformation regarding its static counterpart. A subset of the associated reconstructed thermograms, shown in Figure 11 b) and d), presents a clear step in the 2 intervals highlighted. Even if this steps represent an overfit of the registration, they

are only made apparent in the border of the holes where the image gradients are higher. Thermograms 2 and 4 of d) are affected by the registration overfit.
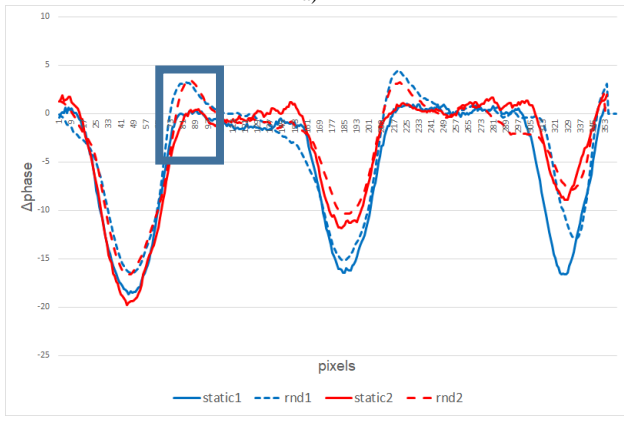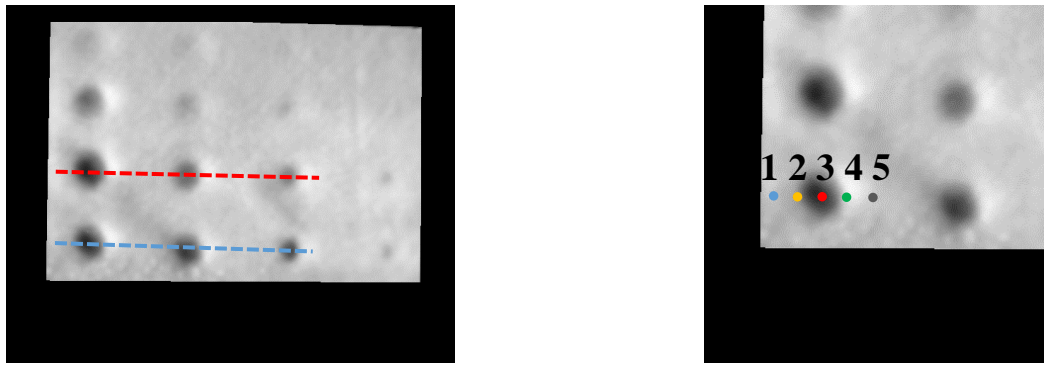

a)

b)

c)

d)

Figure 11. Phase image distortion in edges caused by overfit in registration. a and c) horizontal phase delta profiles with phase highlighted, b and d) thermogram of points in the distorted area, FBH corner points, 2 and 4, magnify the artifact derived from the overfit

This particular problem signals possible avenues in the enhancement of the registration, by weighing the gradients in the optical flow objective function, among others.

In Figure 12 is shown the resulting image-space displacement between frames derived from the stabilization exposed. The misalignments producing the step in the thermograms, do not correspond to any of the spike. This clearly signals the real limitations of the registration smoothing techniques exposed available. Note that each alternating spike in Figure 12 corresponds to the random waypoints of the robot, showing a varying speed, deduced from the registration.
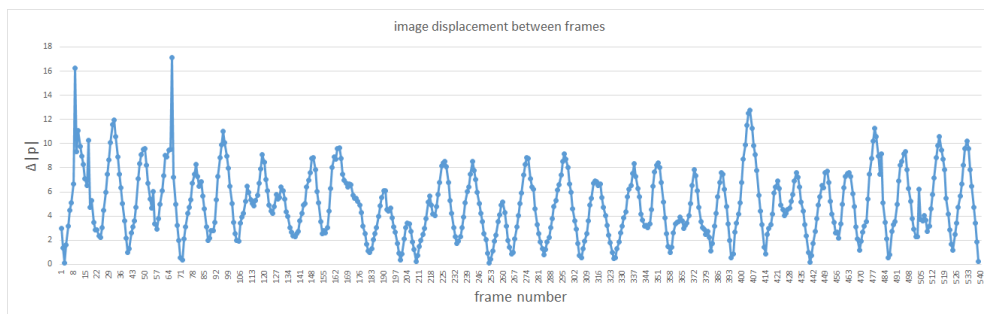

Figure 12. Image-space displacement between frames in random trajectory.

Despite the distortion derived from a localized over fit of the registration, the phase contrast is comparable to the static thermography, leading to the conclusion that a robust stabilization algorithm can enable a viable active thermography inspection.

5.2 Delamination by impact on Eolic blade

Analogous to the work done with FBHs, the comparison has been carried out with the same acquisition and excitation parameters.

Below is a summary of the measurement parameters employed.
- Resolution: 640x512
- Recording speed: 10Hz
- Pulse length: 50s
- Pulse power: 75% (2x2000W)
- Integration time $100\mu s$
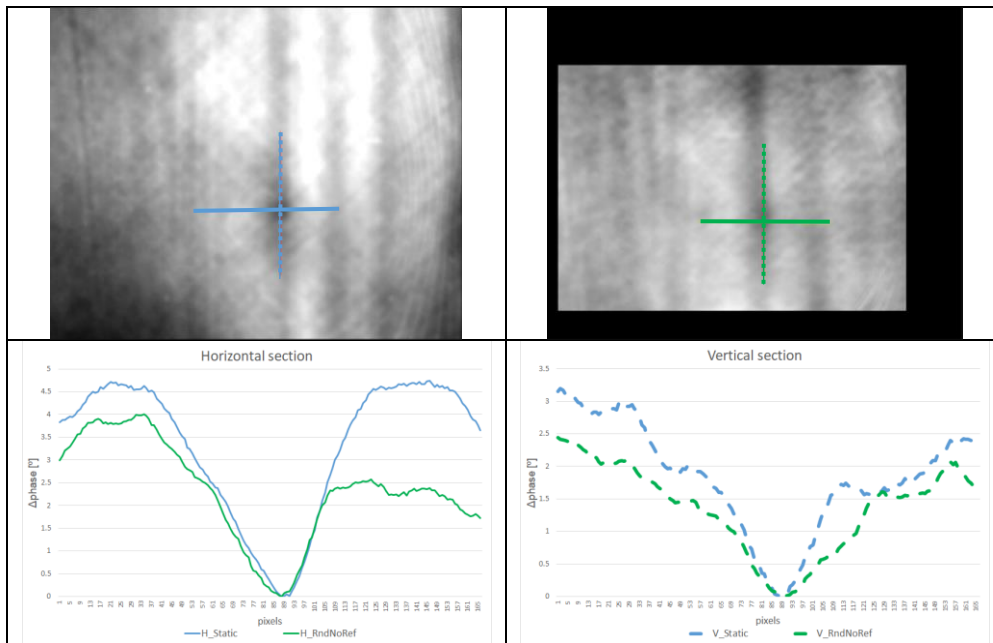- Frame interval FFT evaluation: 500-900 (50-90s, cooling)

Figure 13. Phase image after FFT (0,02 Hz) for static (left) and stabilized (right) sequences

As it can be seen in Figure 13, both static and random stabilized shows a good contrast, even if the phase reduction incurred in the dynamic is noticeable. Contrary to the previous FBH phase profile, this one shows an asymmetric phase contrast reduction in one direction. As previously noted this can be caused by a local registration deviation. Note that the slope of the phase is relatively similar despite its contrast reduction. As it can be seen the delamination defect has been detected in both situations.

5.3 Solar panel

In the solar panel it has not been necessary to carry out a preliminary study to determine optimal parameters. The panel has been connected to the power source and 19V have been applied for each section, inducing an intensity of nine Amps. In the static configuration, still images have been collected with the camera, to later make a total reconstruction of the panel. Figure 14 a hand-stitched result.
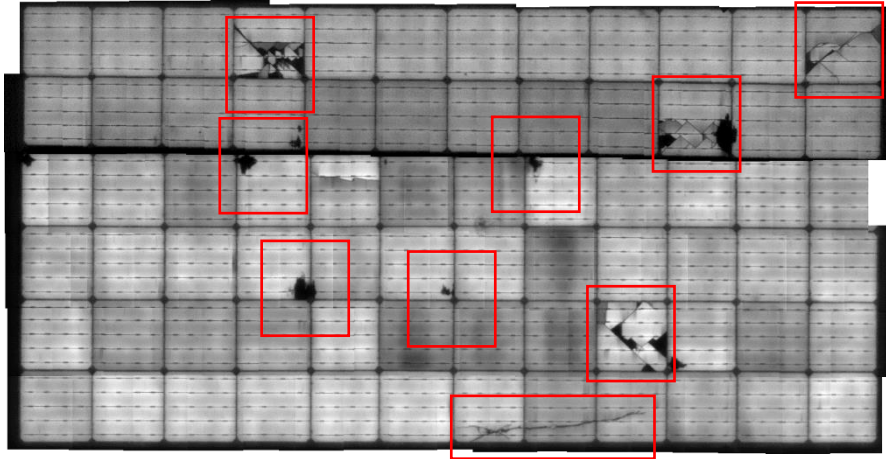
Figure 14. Hand-stitched EL static thermographies with manual defect highlighting

In Figure 14, cracks are plainly visible; these defects can be easily detected by EL. In addition, as the exposure time has been fixed, panels with reduced performance appear darker.

The dynamic test simulating an uneven continuous motion has equally been generated with the robot, following a raster pattern, to which a small sinusoidal component has been added, emulating an imprecise positioning. Contrary to the static configuration, a continuous recording has been made in order to have an automatic reconstruction of the solar panel.

Figure 15 shows the comparison between both configurations (static and dynamic). A small region of the panel has been selected to check that the resolution of the images is as good as on the static approach. Besides this, a zone with no clear edges due to cracked zones has been employed to emphasize the conclusions.
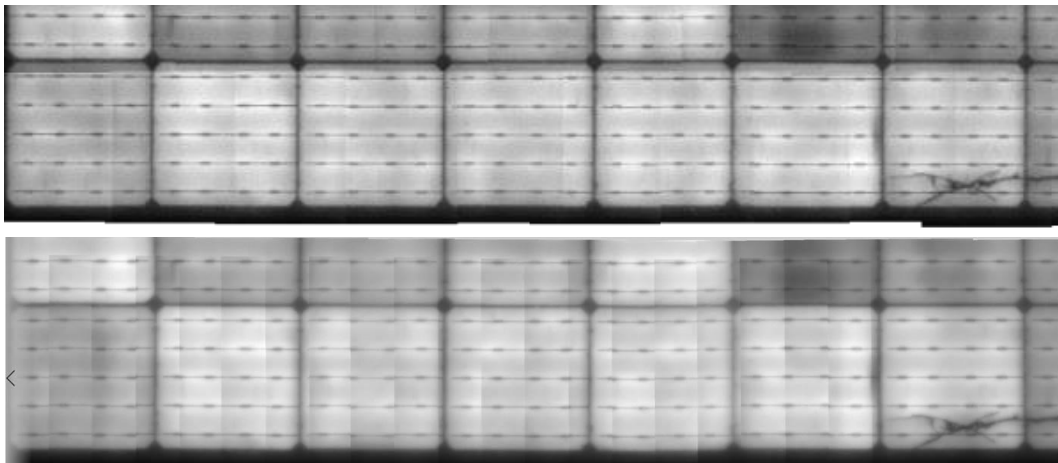

Figure 15. Comparison between hand-stitched frames (top) and automatic (bottom)

6. CONCLUSIONS

Active thermography for the inspection of large composite structures, plane fuselages and wind turbine blades, among others, cannot be automated with conventional means. UAVs present distinctive advantages that should certainly be exploited, but its inherent static motion is one of the main stumbling blocks, towards its use in an active thermography inspection. In this paper, a two-step digital stabilization scheme has demonstrated its efficacy in real defects located in both a wind blade and solar panel. The combination of a feature-based registration algorithm and a dense parametric optical flow direct alignment has enabled the pseudo-static reconstruction of the thermograms.

The adopted experimental methodology, employing a robot with both halogens and IR camera has allowed a direct repeatable comparison of phase images derived from different motions, of the motion stabilized sequence regarding the static thermography one. Comparison in flat bottom holed GFRP sample shows similar phase contrast with marginal differences. Real GFRP wind blade delamination defect, tested with identical motions, have successfully shown the defect itself, albeit with a decreased phase contrast. This reduction is explained by the decreased amount of features and homogeneous gradients of the latter. Repeating the process adhering an artificial mark, produces identical results regarding the static test.

It is important to note that a well-known problem in any image registration system of homogeneous, feature-less surfaces reduces the consistency of the descriptors and, in turn, its accuracy, this has been shown to be a problem, especially in the late cooling phase of thermographies, due to the homogeneity derived from the thermal diffusion.

7. FUTURE WORK

7.1 Active thermography UAV implementation for wind turbine inspection

Carrying out active thermography with an unmanned aerial vehicle (UAV) could be very beneficial for wind turbine inspection, as well as for other inspection tasks. However, there are a number of challenges that would first have to be overcome. The main challenges are perceived to relate to the UAV platform's capability to keep the thermal camera steady enough, the total active thermography payload mass and the active thermography power and energy requirement. It should be possible to overcome these challenges by designing the UAV and its payload along certain characteristics. Responding to those needs is part of the future work.

7.2 Electroluminescence and active thermography systems for solar panels inspection

Together with the electroluminescence inspections developed for the paper, during the European Project DURABLE, several inspections using active thermography for defect detection on solar panels have been made. These inspections can provide interesting results that, combined with Electroluminescence, can achieve a more complete map of defects on the panels. For multi-UAV and multi-UGV scenarios that extend the cooperative setting for solar farms, we plan to build on existing technologies and on cooperation methodologies for autonomous heterogeneous robot fleets, to ensure consistent operation of the UAV + UGV team while carrying out its activities covering the whole farm.

7.3 Digital thermographic stabilization

Future works would need to address this problem by improving the registration pipeline, using weighted optical flow models, global registration techniques and an enhancement of the image-space trajectory post-processing. The generation of a realistic data set, by mounting the setup into a real UAV for the acquisition in varying light conditions, combined with a 3 axis gimbal stabilization device, would allow to reliably model the image-space trajectory and benchmark the system itself. Reflective coatings as well as outdoors light conditions can certainly affect the thermography itself, as well as the digital stabilization. This would ideally be solved with a IR polarization filter. The relative position and orientation of the lamps, as well as the use of parabolic focusing reflectors might also be interesting to investigate, taking into account the reflections and ratio of energy absorbed on the samples. Feature-less homogeneous surface registration can certainly be challenging. This particular aspect would greatly benefit from an increased granularity on the perceived information, for instance polarimetric, multispectral or color infrared cameras would certainly be able to better discern the features previously hidden. Additionally, the possibility of adding reference information into the scene object remains an interesting possibility. Further investigations, need to challenge the system and couple the thermographic setup to a real UAV and UGV.

REFERENCES

[1] M. A. Shohag, E. Hammel, D. Olawale and O. I. Okoli, "Damage mitigation techniques in wind turbine blades: A review," *Wind Engineering,* vol. 41, 5 2017.

[2] A. Sareen, C. Sapre and M. Selig, "Effects of leading edge erosion on wind turbine blade performance," *Wind Energy,* vol. 17, 10 2014.

[3] Y. Ma, P. Martinez-Vazquez and C. Baniotopoulos, "Wind Turbine Tower Collapse Cases: A Historical Overview," *ICE Proceedings Structures and Buildings,* vol. 172, 5 2018.

[4] A. Petraglia and V. Nardone, "Electroluminescence in photovoltaic cell," *Physics Education,* vol. 46, 8 2011.

[5] P. Chaturvedi, B. Hoex and T. M. Walsh, "Broken metal fingers in silicon wafer solar cells and PV modules," *Solar Energy Materials and Solar Cells,* vol. 108, p. 78–81, 2013.

[6] J. Barbedo, "A Review on the Use of Unmanned Aerial Vehicles and Imaging Sensors for Monitoring and Assessing Plant Stresses," *Drones,* vol. 3, p. 40, 4 2019.

[7] F. Ellrich, M. Bauer, N. Schreiner, A. Keil, T. Pfeiffer, J. Klier, S. Weber, J. Jonuscheit, F. Friederich and D. Molter, "Terahertz quality inspection for automotive and aviation industries," *Journal of Infrared, Millimeter, and Terahertz Waves,* vol. 41, p. 470–489, 2020.

[8] L. REOCREUX, Y. U. Zhewei, S. ARNOULD and P. R. O. N. Hervé, "Passive thermography for delamination detection in GFRP of Wind Turbine Blade," 2020.

[9] C. Konukseven, O. Atiz, S. Alcay and S. Ogutcu, "Analysis of the contribution of the multi-GNSS to long-distance RTK," 2020.

[10] T. Sakagami and S. Kubo, "Application of pulse heating thermography and Lock-In thermography to quantitative non-destructive evaluations," *Infrared Physics & Technology,* vol. 43, pp. 211-218, 6 2002.

[11] M. Dhimish and V. Holmes, "Solar cells micro crack detection technique using state-of-the-art electroluminescence imaging," *Journal of Science: Advanced Materials and Devices,* vol. 4, 11 2019.

[12] N. Mathias, F. Shaikh, C. Thakur, S. Shetty, P. Dumane and S. Chavan, "Detection of Micro-Cracks in Electroluminescence Images of Photovoltaic Modules," *SSRN Electronic Journal,* 1 2020.

[13] M. Fonder and M. Droogenbroeck, "Mid-Air: A Multi-Modal Dataset for Extremely Low Altitude Drone Flights," 2019.

[14] A. Antonini, W. Guerra, V. Murali, T. Sayre-McCord and S. Karaman, "The blackbird dataset: A large-scale dataset for uav perception in aggressive flight," in *International Symposium on Experimental Robotics*, 2018.

[15] E. Schneider, T. Villgrattner, J. Vockeroth, K. Bartl, S. Kohlbecher, S. Bardins, H. Ulbrich and T. Brandt, "EyeSeeCam: An Eye Movement-Driven Head Camera for the Examination of Natural Visual Exploration," *Annals of the New York Academy of Sciences,* vol. 1164, pp. 461-7, 6 2009.

[16] M. Drahanský, F. Orság and P. Hanacek, "Accelerometer Based Digital Video Stabilization for Security Surveillance Systems," 2009.

[17] F. Khodayar, F. Lopez, C. Ibarra-Castanedo and X. Maldague, "Optimization of the inspection of large composite materials using robotized line scan thermography," *Journal of Nondestructive Evaluation,* vol. 36, p. 32, 2017.

[18] N. Schuster and J. Franks, "Depth of field in modern thermal imaging," in *Infrared Imaging Systems: Design, Analysis, Modeling, and Testing XXVI*, 2015.

[19] E. Rosten and T. Drummond, "Fusing points and lines for high performance tracking," in *Tenth IEEE International Conference on Computer Vision (ICCV'05) Volume 1*, 2005.

[20] E. Rublee, V. Rabaud, K. Konolige and G. Bradski, "ORB: An efficient alternative to SIFT or SURF," in *2011 International conference on computer vision*, 2011.

[21] D. G. Lowe, "Object recognition from local scale-invariant features," 1999.

[22] C. Kuglin and D. Hines, "The Phase Correlation Image Alignment Method," *IEEE International Conference on Cybernetics and Society,* 1 1975.

[23] B. D. Lucas, T. Kanade and others, "An iterative image registration technique with an application to stereo vision," 1981.

[24] M. J. Black and A. Rangarajan, "On the unification of line processes, outlier rejection, and robust statistics with applications in early vision," *International journal of computer vision,* vol. 19, p. 57–91, 1996.

[25] F. Dellaert and R. Collins, "Fast Image-Based Tracking by Selective Pixel Integration," 3 2000.

[26] S. Baker and I. Matthews, "Lucas-Kanade 20 Years On: A Unifying Framework Part 1: The Quantity Approximated, the Warp Update Rule, and the Gradient Descent Approximation," *International Journal of Computer Vision - IJCV,* 1 2004.

[27] J.-Y. Bouguet and others, "Pyramidal implementation of the affine lucas kanade feature tracker description of the algorithm," *Intel corporation,* vol. 5, p. 4, 2001.

[28] L. Alvarez, J. Weickert and J. Sánchez, "Reliable Estimation of Dense Optical Flow Fields with Large Displacements," *International Journal of Computer Vision,* vol. 39, pp. 41-56, 8 2000.

[29] S. Pant, P. Nooralishahi, N. Avdelidis, C. Ibarra-Castanedo, M. Genest, S. Deane, J. Valdes, A. Zolotas and X. Maldague, "Evaluation and Selection of Video Stabilization Techniques for UAV-Based Active Infrared Thermography Application," *Sensors,* vol. 21, p. 1604, 2 2021.

[30] R. Yang, Y. he and H. Zhang, "Progress and trends in nondestructive testing and evaluation for wind turbine composite blade," *Renewable and Sustainable Energy Reviews,* vol. 60, pp. 1225-1250, 7 2016.